Experimental Characterization of the MIMO Wireless Channel: Data Acquisition and Analysis

Jon W. Wallace, Michael A. Jensen, A. Lee Swindlehurst, and Brian D. Jeffs

Abstract— **Detailed performance assessment of space-time coding algorithms in realistic channels is critically dependent upon accurate knowledge of the wireless channel spatial characteristics. This paper presents an experimental measurement platform capable of providing the narrowband channel transfer matrix for wireless communications scenarios. The system is used to directly measure key multiple-input multiple-output (MIMO) parameters in an indoor environment at 2.45 GHz. Linear antenna arrays of different sizes and construction with up to 10 elements at transmit and receive are utilized in the measurement campaign. This data is analyzed to reveal channel properties such as transfer matrix element statistical distributions and temporal and spatial correlation. Additionally, the impact of parameters such as antenna element polarization, directivity, and array size on channel capacity are highlighted. The paper concludes with a discussion of the relationship between multipath richness and path loss as well as their joint role in determining channel capacity.**

Keywords— **MIMO channels, indoor channels, measured channel data**

I. Introduction

THE increasing demand for capacity in wireless systems has motivated considerable research aimed at achieving higher throughput on a given bandwidth. One important finding of this activity is the recent demonstration that for an environment sufficiently rich in multipath components, the wireless channel capacity can be increased using multiple antennas on both transmit and receive sides of the link [1]–[5]. For example, recent research results have demonstrated data rates as high as 40 bits/s/Hz in an indoor environment [6]. Algorithms that achieve this increased capacity actually *exploit* the multipath structure by cleverly coding the data in both time and space. Therefore, in order to assess the performance of systems that implement these algorithms, we must gain an improved understanding of the complex *spatial* behavior of wireless multiple-input multiple-output (MIMO) channels [7].

Past methods for characterizing multipath MIMO channels include approximate statistical analyses [1] and ray tracing procedures [8]. These solutions offer information concerning the general channel behavior but suffer from their inability to accommodate an adequately detailed representation of the propagation environment. More recently, experimental measurement campaigns have been initiated in order to statistically characterize both indoor and outdoor wireless MIMO channels [9]–[11]. Results from these experiments have provided considerable insight concerning the capacity increases possible using MIMO systems.

In this work, we report the development of and results from an experimental platform designed to probe the transfer matrix for indoor MIMO channels. This system is used to obtain narrowband channel transfer matrix data at 2.45 GHz using two different linear arrays: one with 4 dual-polarization elements and one with 10 single polarization elements. The key aspects of the hardware system are presented, including a discussion of measurement issues and data processing methodologies. Representative data obtained with the instrument in several indoor environments are also provided, with emphasis placed on key parameters such as channel stationarity, transfer matrix element statistics, and channel spatial correlation. Additionally, the paper highlights the effect of such factors as antenna element polarization and directivity on the capacity, and illustrates the decrease in capacity per antenna that occurs as the array size increases. Finally, a discussion is provided concerning the relationship between multipath richness and path loss as well as their joint role in determining channel capacity.

The authors are with the Department of Electrical and Computer Engineering, 459 Clyde Building, Brigham Young University, Provo, UT 84602. This work was supported by the National Science Foundation under Wireless Initiative Grant CCR 99-79452 and Information Technology Research Grant CCR-0081476.

II. Measurement System

Experimental probing of the MIMO wireless channel involves measuring the transfer matrix $\mathbf{H}$, where the element $H_{mn}(\omega)$ represents the frequency dependent transfer function between the n^{th} transmitter and m^{th} receiver antennas. The experimental platform, depicted in Figure 1, uses a custom narrowband MIMO communications system operating with a center frequency between 0.8 and 6 GHz [12]. For this work, a center frequency of 2.45 GHz has been chosen. The system operates by transmitting N uniquely-coded and co-channel binary phase shift keyed (BPSK) signals from N distinct antennas. The receiver downconverts the signal from each of the M antennas and stores the resulting sequences on a PC for post-processing. The system can accommodate up to N = 16 transmit and M = 16 receive antenna elements although only 10 channels are used in this study. A calibration procedure is applied before data collection to remove the effects of unequal channel gains and phases in the transmitter and receiver hardware. The calibration coefficients obtained are applied during the data post-processing.

A. Transmitter

The transmit system consists of a custom radio frequency (RF) subsystem that accepts binary sequences from an external digital pattern generator and a local oscillator (LO) signal from a tunable microwave source. The subsystem distributes these signals to 16 individual cards, each of which amplifies the LO signal and multiplies it with one of the binary sequences to produce BPSK modulation. The resulting signal is amplified to 0.5 W and fed to one of the N transmit antennas. The pseudorandom binary sequences used in the system are constructed using

a shift-generator initialized with a maximum-length sequence polynomial. The resulting codes have good correlation properties but are not perfectly orthogonal, necessitating the channel inversion technique discussed in Section III-C.

B. Receiver

The receive system consists of a second RF subsystem that accepts a LO signal from a microwave source. Each of 16 receive cards amplifies, downconverts, and filters the signal from one of the M receive antennas. The resulting intermediate frequency (IF) signals are sampled on a 16-channel 1.25 Msample/s analog-to-digital (A/D) conversion card for storage on the PC. This data is then post-processed according to the procedures outlined below.

III. Data Processing

The raw data collected using the measurement platform is processed to obtain estimates of the time-variant channel matrix. The technique consists of 3 basic steps: (1) code synchronization, (2) carrier recovery, and (3) channel estimation.

A. Code Synchronization

Locating the start of the modulating codes begins by correlating the signal from one of the M receive antennas with a baseband representation of one of the transmit codes. A Fast Fourier Transform (FFT) of this result produces a peak at the IF when the known code and the code in the receive signal are aligned. The algorithm expedites the process by using shortened correlating codes and coarse steps at the beginning of the search process, and adaptively reducing the step size and switching to full-length codes as the search converges. Additionally, if the signal carrying the specified code is weak, the maximum correlation may not occur at code alignment. To overcome this, our procedure searches over every combination of receive channel and code to ensure accurate code synchronization.

B. Carrier Recovery

The FFT peak obtained during code synchronization provides an estimate of the IF. This result is refined using a subplex optimization loop that maximizes the magnitude of the Discrete Time Fourier Transform (DTFT) of the despread signal (known aligned code multiplied by the receive signal). Following frequency estimation, the phase variation is recovered by moving a window along the despread signal and correlating this waveform against a complex sinusoid at the IF, as shown in Figure 2. The phase of this result represents the phase at the center of the recovery window. An averaging window is then used to smooth this phase estimate.

C. Channel Estimation

Because the pseudorandom codes used in the probing system are not strictly orthogonal, it is necessary to perform an inversion to extract the complex channel transfer matrix from the measured data. This inversion is formulated by first recognizing that the IF signal on the m^{th} receive channel is composed of N BPSK codes, with each code represented by an amplitude A_{mn} and phase ϕ_{mn}. If $p_n[k]$ represents the k^{th} sample of the n^{th} code, the discrete received signal is given as

$$y_m[k] = \sum_{n=1}^{N} A_{mn} p_n[k] \cos(\Omega_1 k + \phi_k + \phi_{mn}) + \eta[k] \quad (1)$$

where Ω_1 is the discrete (recovered) carrier frequency, ϕ_k is the randomly varying carrier phase, and $\eta[k]$ represents the discrete noise sample that is assumed to be spectrally white with a zero-mean Gaussian amplitude distribution.

To construct channel matrices, we must infer channel parameters A_{mn} and ϕ_{mn} from the sequence $y_m[k]$. To this end, consider forming an estimate of these parameters based upon $K = k_2 - k_1 + 1$ samples of the sequence (corresponding to the code length). Also assume that $\hat{y}_m[k]$ is the observed signal. Using the zero-mean Gaussian distribution of the noise, the maximum likelihood estimation (MLE) of the channel parameters results from finding the values of $\widetilde{A}_{mn} = A_{mn} e^{j\phi_{mn}} = A^R_{mn} + jA^I_{mn}$ that minimize the expression

$$T_m = \sum_{k=k_1}^{k_2} \left\{ \hat{y}_m[k] - \mu_{mk} \right\}^2 \quad (2)$$

where

$$\mu_{mk} = \sum_{n=1}^{N} \left\{ A^R_{mn} \cos(\Omega_1 k + \phi_k) - A^I_{mn} \sin(\Omega_1 k + \phi_k) \right\} p_n[k]. \quad (3)$$

In order to determine the MLE values of $\widetilde{A}_{mn}$, we take the derivative of T_m with respect to both $A^R_{m\ell}$ and $A^I_{m\ell}$, $1 \le \ell \le N$, and set the result to zero. Performing this operation produces the equations

$$2 \sum_{k=k_1}^{k_2} \hat{y}_m[k] p_\ell[k] \cos(\Omega_1 k + \phi_k) = \sum_{k=k_1}^{k_2} \sum_{n=1}^{N} p_n[k] p_\ell[k] \left\{ A^R_{mn}(1 + \alpha_k) - A^I_{mn} \beta_k \right\} \quad (4)$$

$$2 \sum_{k=k_1}^{k_2} \hat{y}_m[k] p_\ell[k] \sin(\Omega_1 k + \phi_k) = \sum_{k=k_1}^{k_2} \sum_{n=1}^{N} p_n[k] p_\ell[k] \left\{ A^I_{mn}(1 - \alpha_k) - A^R_{mn} \beta_k \right\} \quad (5)$$

where $1 \le m \le M$, $1 \le \ell \le N$, $\alpha_k = \cos[2(\Omega_1 k + \phi_k)]$ and $\beta_k = \sin[2(\Omega_1 k + \phi_k)]$. These equations can now be formed into the block matrix equation

$$\begin{bmatrix} \overline{D}^R_m \\ \overline{D}^I_m \end{bmatrix} = \begin{bmatrix} \mathbf{B}_{11,m} & \mathbf{B}_{12,m} \\ \mathbf{B}_{21,m} & \mathbf{B}_{22,m} \end{bmatrix} \begin{bmatrix} \overline{A}^R_m \\ \overline{A}^I_m \end{bmatrix}. \quad (6)$$

The channel matrix elements are given by $H_{mn} = \widetilde{A}_{mn}$.

IV. Channel Matrix Characteristics

The measurement system was deployed on the fourth-floor of the five-story engineering building on the Brigham Young

University campus. This building, constructed with cinderblock partition walls and steel-reinforced concrete structural walls contains classrooms, laboratories, and several small offices. Data were collected at a center frequency of 2.45 GHz using 1000-bit binary codes at a chip rate of 12.5 kbps, yielding a nominal bandwidth of 25 kHz. This narrow bandwidth is clearly not representative of most modern communications systems, and therefore additional work is required to fully characterize the frequency behavior of the MIMO channel matrix. However, the results obtained can be used to assess the channel spatial behavior and temporal variation as well as the effect of antenna characteristics on the achievable channel capacity.

The 12.5 kbps chip rate produces one channel matrix estimate every 80 ms, where the estimate represents the average channel response over the code length. Because channel changes occur on the time scales of relatively slow physical motion (people moving, doors closing, etc.), this sample interval is adequate for the indoor environment under investigation (see Section IV-B for a discussion of channel temporal variation). Shorter codes could be used to reduce this time if necessary. Alternatively, a higher speed data acquisition system could be employed in conjunction with a higher chip rate to decrease the time between channel estimates.

Table I lists the five different locations for the transmit and receive subsystems used in this study. Rooms 400 and 484 are central labs in the building separated by a hallway (designated as "Hall"). "5 rooms" and "Many Rooms" in the table indicate that the receiver was placed at several locations in different rooms. The specific linear antenna arrays employed were 4 element single polarization patches with $\lambda/2$ spacing (4SP), 2 element dual polarization (V/H) patches with $\lambda/2$ spacing (2DP), and 10 element monopole antennas with $\lambda/4$ spacing (10SP). Data records were each 10-s long.

Since the actual received power varies as a function of the transmit and receive locations, some type of channel normalization is required to facilitate comparison of the results. One reasonable normalization is to scale the channel matrices such that on average, the power transfer between a single transmit and single receive antenna is unity. To see this, let $\hat{\mathbf{H}}^{(k)}$ and $\mathbf{H}^{(k)}$ represent the observed and normalized matrices, respectively, where the superscript denotes the index of the matrix sample in time. Using A to represent a normalization constant such that $\mathbf{H}^{(k)} = A\hat{\mathbf{H}}^{(k)}$, the unity average power gain constraint may be expressed as

$$\frac{1}{KMN}\sum_{k=1}^{K}\sum_{m=1}^{M}\sum_{n=1}^{N}|A\hat{H}_{mn}^{(k)}|^2 = 1 \tag{7}$$

where K is the total number of matrix samples. Solving this equation for A leads to

$$A = \left(\frac{1}{KMN}\sum_{k=1}^{K}\sum_{m=1}^{M}\sum_{n=1}^{N}|\hat{H}_{mn}^{(k)}|^2\right)^{-\frac{1}{2}}. \tag{8}$$

If the K matrix samples include the entire data set under consideration, this scaling allows assessment of the effects of path loss on the channel characteristics. If, on the other hand, $K = 1$ is used, each individual matrix will produce the same signal-to-noise ratio (SNR). This is useful when assessing the impact of antenna parameters such as polarization, directivity, or array size on capacity. In this paper, therefore, data is normalized using $K = 1$ unless specifically stated in the discussion.

Finally, it is important to assess the dynamic range of the receiver system. To accomplish this, the carrier modulated with a single code was directly injected into each receive channel and the channel estimation procedure was applied. The carrier power was varied linearly until saturation occurred at high power and until the carrier estimation procedure failed at low power. Figure 3 shows the response from one of the channels (all channels were within $\pm$1dB of each other). This plot also contains a histogram of the received power level for all measurements used in this work. These results imply that the effective SNR for most measurements is above 40dB and never falls below 20dB. It is important to point out that error in the carrier recovery introduces about 1% error, producing an upper bound of 40dB on the effective channel SNR. This high SNR level implies that the statistical channel properties will be minimally influenced by the noise.

A. Channel Matrix Element Statistics

We begin this study by presenting the marginal probability density functions (PDF) for the magnitude and phase of the elements of $\mathbf{H}$. These empirical PDFs are computed according to

$$p_{mag}[x] = \frac{1}{KMN\Delta x}\underset{K,M,N}{\mathrm{HIST}}(|H_{mn}^{(k)}|, \Delta x) \tag{9}$$

$$p_{pha}[x] = \frac{1}{KMN\Delta x}\underset{K,M,N}{\mathrm{HIST}}(\angle H_{mn}^{(k)}, \Delta x) \tag{10}$$

where $\mathrm{HIST}(f, \Delta x)$ represents a histogram of the function f with bins of size Δx and K is the number of $\mathbf{H}$ matrix samples. In this case histograms are computed by treating each combination of matrix sample, transmit antenna, and receive antenna as an observation.

Figures 4 and 5 show the empirical PDFs for sets 4×4(a) and 10×10(a) respectively. These results are compared with the Rayleigh distribution (magnitude) with parameter $\sigma^2 = 0.5$ and the uniform distribution (phase) on $[-\pi,\ \pi]$. The agreement between the analytical and empirical PDFs is excellent. The improved fit for 10×10 data arises from more records and antennas available.

B. Channel Temporal Correlation

Because the indoor channel is subject to temporal drift due to motion of people, doors, etc., it is interesting to explore the time scales over which these changes occur. This study can be accomplished by examining the temporal autocorrelation function for each element of the transfer matrix. The average autocorrelation is given as

$$X_\ell = \langle H_{mn}[k]H_{mn}^*[k+\ell]\rangle \tag{11}$$

where k is a time sample, ℓ is a sample shift, and $< \cdot >$ represents an average over all combinations of transmit antenna, receive antenna, and starting time sample. This averaging includes

all 10-second records for the data set under investigation. The temporal correlation coefficient is then given by $\rho_\ell = X_\ell / X_0$.

Figure 6 plots the magnitude of ρ_ℓ over a period of 5 seconds for each of the data sets considered. We observe that for all measurements, the correlation remains relatively high. This is significant, as it provides insight into the required frequency of training events for MIMO algorithms that use channel state information. We also note that the temporal correlation seems to exhibit an exponential decay to a "resting" value, suggesting that the mean of the channel elements remains relatively constant over the 5-s interval. This behavior is reasonable, since channel disturbances tend to be temporary, causing the channel transfer function to oscillate about a constant value. Over longer periods of time, the correlation will likely decrease more substantially due to more permanent changes in the channel.

The variation in ρ_ℓ for the different data sets considered is directly related to the measurement conditions. For example, the 10×10(a) and 4×4(a) data sets were taken during periods of very low activity and the data sets were large, resulting in good statistical averages. In contrast, sets 10×10(c) and 4×4(b) were both taken during the middle of the day when activity was higher. Nearly half of the measurements in the 10×10(b) data set involved continuous movement of the receiver or transmitter during acquisition, producing the more rapid decrease in correlation values.

C. Channel Spatial Correlation

The channel spatial correlation is an important physical mechanism since lower signal correlation between adjacent antennas tends to produce higher average channel capacity. To examine the channel spatial behavior, we assume a correlation function that is separable in transmit and receive, or

$$R(m,n;i,j) = \mathrm{E}[H_{mn}H_{ij}^*] = R_R(m,i)R_T(n,j) \qquad (12)$$

where the transmit and receive correlation functions are given by

$$R_T(n,j) = \frac{1}{M}\sum_{m=1}^{M}\mathrm{E}[H_{mn}H_{mj}^*] \qquad (13)$$

$$R_R(m,i) = \frac{1}{N}\sum_{n=1}^{N}\mathrm{E}[H_{mn}H_{in}^*] \qquad (14)$$

and $\mathrm{E}[\cdot]$ is an expectation. The transmit and receive correlation functions are computed empirically by replacing the expectation with an average over all time samples.

Figure 7 shows the shift-invariant spatial transmit and receive correlation coefficient compared with Jakes' model [13] where $R_R(i,j) = R_T(i,j) = J_0(2\pi|i-j|\Delta z_\lambda)$ and Δz_λ is the antenna separation in wavelengths. Data sets 4×4(a) and 10×10(a) were used for this example. For this shift-invariant case, we treat all pairs of antennas with the same spacing as independent observations. For small separation, the agreement between the experimental correlation and Jakes' model is very good. The disparity at higher separations is likely due to non-uniform angle of arrival of multipath components as well as a reduced amount of available data for computing the correlation statistics.

The correlation values obtained from this analysis represent the temporal cross correlation function at zero time offset. We have computed the full temporal cross correlation function for the data collected here using an analysis similar to that of Section IV-B. Comparing this result to the average temporal *auto-correlation* function of Eq. (11) scaled by the spatial correlation value shown in Figure 7 for the appropriate antenna separation shows that the two functions are always within 5% and usually within 1%. This observation suggests that Figures 6 and 7 completely specify the average correlation behavior of the data.

V. Channel Capacity

The channel statistical properties are interesting as they lend insight into mechanisms for exploiting the increased capacity of the environment using MIMO architectures. Ultimately, however, channel capacity, or the upper bound on achievable data rates for the channel, is the key parameter of interest. In this study, capacities are computed from the measured $\mathbf{H}$ matrices according to the water filling solution of the channel orthogonalized by the singular value decomposition (SVD) [5], [14]. This formulation yields the absolute upper bound on channel capacity which can be expressed as

$$C = \sum_{i=1}^{q}\log_2\left(1+\tilde{Q}_{ii}\lambda_i\right) \qquad (15)$$

$$\tilde{Q}_{ii} = \left[\frac{1}{q}\left(\frac{P_T}{\sigma^2}+\sum_{j=1}^{q}\frac{1}{\lambda_j}\right)-\frac{1}{\lambda_i}\right]^+ \qquad (16)$$

where $[z]^+ = \max(0,z)$ and λ_i is the squared magnitude of the ith singular value of $\mathbf{H}$ when these singular values are sequenced in descending order. P_T is the total transmit power, and σ^2 represents the single receiver noise variance (additive white Gaussian noise is assumed). The integer q represents the number of non-zero values of $\tilde{Q}_{ii}$. Since q appears in the expression of Eq. (16), $\tilde{Q}_{ii}$ must be repeatedly computed for $q = 1$ to $\min(M,N)$. The value of q used in the capacity computation is then the largest value of q such that all $\tilde{Q}_{ii} > 0$, $1 \le i \le q$. It is important to recognize that due to the normalization given in Section IV, P_T/σ^2 represents the single-input single-output (SISO) SNR, which is held at 20dB for all capacity computations that follow. Also, capacity is given in the standard units of bits per channel use (bits/use) [14] which can be interpreted here as bits/s/Hz.

A. Polarization Dependence

The linear patch arrays employed in the measurements consist of four dual-polarization elements. In order to assess the role of polarization in the performance of MIMO architectures, we used four transmit/receive channels (set 4×4(b)) to excite both V and H feeds on two $\lambda/2$ separated patches on each side of the link. By looking at the appropriate submatrices of $\mathbf{H}$, the complimentary cumulative distribution functions (CCDFs) of capacity can be compared for three different 2×2 sub-channels: (1) 2 elements with same polarization (V or H) but separated by $\lambda/2$, (2) 2 elements which have orthogonal polarization and are colocated, and (3) 2 elements which have both orthogonal polarization and are separated by $\lambda/2$.

Figure 8 shows the results of this study. Two single polarization elements (SP) is the inferior case, due to correlation between the elements. The next line on the graph (IID) is the capacity for a 2×2 channel matrix with independent identically distributed (i.i.d.) complex Gaussian elements with unit variance, the capacity being computed using Monte Carlo over 10^6 channel realizations. The capacities for the dual polarized elements (DP) and dual polarized elements with separation (DPS) are virtually identical. The fact that the dual polarized elements outperform the IID case seems extraordinary at first glance. However, it is a well-known phenomenon that coupling between the orthogonal polarizations will be small, presenting an $\mathbf{H}$ matrix which is nearly diagonal. The final line (DIAG) shows the performance when $\mathbf{H}$ has i.i.d. complex Gaussian elements on the diagonal but is identically zero everywhere else (computed in a manner similar to IID). As expected, this case outperforms our dual-polarization elements which exhibit weak correlation.

The channel matrix normalization applied in Figure 8 ensures that each 2×2 sub-channel has the same SISO SNR. This type of normalization is perhaps optimistic, since low transmission between the orthogonally polarized channels will translate into reduced average receive SNR. A more realistic comparison takes each 4×4 channel matrix and normalizes to achieve an average SISO SNR of 20 dB over the co-polarized matrix elements only. The 2×2 sub-channels are then formed *after* this normalization, preserving the relative receive power of the sub-channels. Figure 9 depicts the CCDFs resulting from measured data and from Monte Carlo simulations of two ideal cases. In the simulations, 4×4 channel matrices are generated having i.i.d. complex Gaussian co-polarized elements, with the cross-polarized elements set to zero. The new normalization is applied to the simulated channels, and 2×2 single-polarization (sSP) and dual polarization (sDP) sub-channels are formed.

The conclusions drawn from Figure 9 are quite different from those drawn from Figure 8. First, we note that the slopes in the new plot are more gradual because the power in the sub-channels has higher variance (only the entire 4×4 matrix is constrained). Second, in the simulations sSP clearly outperforms sDP due to the advantage in receive SNR. For the measured data, however, the spatially separated elements have nonzero coupling, and the increased capacity due to nearly orthogonal channels offsets the degradation from reduced receive SNR. Thus, for compact arrays of closely spaced elements, dual-polarization is an attractive choice. However, when wide separation is possible, spatially separated elements are more attractive due to the power advantage.

B. Directivity Dependence

The monopole antennas employed radiate uniformly in the plane perpendicular to the antennas. The patch antennas, on the other hand, only radiate into a half space. These two types of antennas allow examination of the effect of antenna directivity on channel capacity. Figure 10 plots the capacity of the 4×4 channel for four patch antennas (transmit and receive) from set 4×4(a) and for four monopole antennas using subsets of set 10×10(a). These results indicate that the omnidirectional antennas slightly outperform the more directive patch antennas. This result may be somewhat misleading due to the normalization of $\mathbf{H}$. It is reasonable that since the monopoles are omnidirectional, they receive more multipath components, resulting in higher capacity. However, the reduced multipath richness in the directional case is potentially offset by the improved SNR resulting from the increased antenna gain, allowing a higher data rate than in the omnidirectional case. This second effect is ignored since the $\mathbf{H}$ matrices are normalized to a specified SISO SNR. The similarity of the CCDFs suggests that even though the patch antennas exhibit reduced angular field of view, the multipath is nearly as rich as the omnidirectional case for a small number of antennas.

C. Dependence on Number of Antennas

Naturally, it is not anticipated that the capacity will continue to grow indefinitely as more antenna elements are added. To explore this behavior, we examine the dependence of capacity on the number of antennas for 2, 4, and 10 monopole transmit and receive antennas. To make a fair comparison, each array in the study possesses the same total length (2.25λ). This study uses the data from set 10×10(a). Figure 11 shows the capacity CCDFs per number of transmit and receive antennas. Also, Monte Carlo simulations were performed to obtain capacity CCDFs for channel matrices having i.i.d. complex Gaussian elements with unit variance. These results indicate an excellent agreement between the measured 2×2 and ideal 2×2 (independent Gaussian) channel due to the very wide separation of the antennas (2.25λ). The ideal case predicts that the capacity per antenna should approach a constant as the number of antennas becomes large. Measurement shows, however, that as we pack more antennas into our array, the capacity per antenna drops, due to higher correlation between adjacent elements.

D. Path Loss Dependence

Studies on the capacity of the MIMO channel often focus on the gains due to multipath interference and ignore the reduction in SNR due to path loss. In a hypothetical indoor wireless MIMO system, as separation between transmit and receive increases, capacity increases due to increased channel complexity (multipath). However, path loss also increases, leading to lower SNR and therefore reduced capacity. This interesting tradeoff deserves some attention [11].

To highlight the importance of path loss, a study was performed with several transmit and receive scenarios as depicted in Figure 12. The transmit and receive arrays are the same linear monopole arrays with $\lambda/4$ element separation as mentioned before. A total of 7 transmit/receive locations were possible, and $\mathbf{H}$ for several combinations was probed. Each arrow in the figure represents a single scenario with the arrow pointing from transmit location to receive location. The top number in the box on each arrow gives the channel capacity using the standard single $\mathbf{H}$ matrix normalization ($K = 1$ in Eq. (8)) for 20dB SNR. The second number (in italics) gives the capacity when the normalization is applied over *all* $\mathbf{H}$ matrices in the study for an average SISO SNR of 20dB. This second value includes the capacity degradation due to path loss.

Several of the cases with large separation ($5 \rightarrow 3$, for example) exhibit a high capacity when path loss excluded (due to large multipath), but suffer greatly when this loss is included.

Other cases where transmit and receive are in closer proximity ($7 \rightarrow 4$ most notably) exhibit the opposite effect due to the high SNR observed. These results demonstrate the importance of including both path loss and multipath richness when comparing the performance of different channels.

VI. Conclusion

Wireless communication systems employing multiple transmit and receive antennas have potentially greater capacity than their single antenna counterparts on the same bandwidth. Understanding the gains that are possible with such systems requires detailed knowledge of the MIMO channel transfer matrix. This paper has presented narrowband MIMO measurements of the indoor channel at 2.45 GHz for arrays with up to 10 antenna elements. Details of the required hardware and data processing were outlined along with representative data. The measured data were presented so as to allow assessment of the channel statistical behavior including transfer matrix PDFs and temporal and spatial correlation. Additionally, the impact of polarization, directivity, and number of array elements on channel capacity has been demonstrated. Finally, the importance of including both path loss and multipath richness when comparing capacity of different wireless channels has been illustrated. These results should provide invaluable insight into the behavior of MIMO wireless channels.

References

[1] G. J. Foschini and M. J. Gans, "On limits of wireless communications in a fading environment when using multiple antennas," *Wireless Personal Communications*, vol. 6, no. 3, pp. 311–335, March 1998.

[2] T. L. Marzetta and B. M. Hochwald, "Capacity of a mobile multiple-antenna communication link in Rayleigh flat fading," *IEEE Trans. Information Theory*, vol. 45, no. 1, pp. 139–157, May 1999.

[3] V. Tarokh, N Seshadri, and A. R. Calderbank, "Space-time codes for high data rate wireless communication: Performance criterion and code construction," *IEEE Trans. Information Theory*, vol. 44, no. 2, pp. 744–65, March 1998.

[4] P. Wolniansky, G. Foschini, G Golden, and R. Valenzuela, "V-BLAST: An architecture for realizing very high data rates over the rich scattering wireless channel," in *Proceedings of IEEE ISSSE-98*, Pisa, Italy, Sep. 1998.

[5] G. G. Raleigh and J. M. Cioffi, "Spatio-temporal coding for wireless communication," *IEEE Transactions on Communications*, vol. 46, pp. 357–366, Mar. 1998.

[6] G. Golden, C Foschini, R Valenzuela, and P. Wolniansky, "Detection algorithm and initial laboratory results using V -BLAST space-time communication architecture," *Electronic Letters*, vol. 35, no. 1, pp. 14–15, Jan. 1999.

[7] Q. Spencer, B. Jeffs, M. Jensen, and A. Swindlehurst, "Modeling the statistical time and angle of arrival characteristics of an indoor multipath channel," *IEEE J. Selected Areas Commun.*, vol. 18, no. 3, pp. 347–360, Mar. 2000.

[8] G. Athanasiadou, A. Nix, and J. McGeehan, "A microcellular ray-tracing propagation model and evaluation of its narrow-band and wide-band predictions," *IEEE J. Selected Areas Commun.*, vol. 18, no. 3, pp. 322–335, Mar. 2000.

[9] C. C. Martin, J. H. Winters, and N. R. Sollenberger, "Multiple-input multiple-output (MIMO) radio channel measurements," in *IEEE Vehicular Technology Conference (Fall VTC 2000)*, Boston, MA, Sep 2000, vol. 2, pp. 774–779.

[10] J. P. Kermoal, L. Schumacher, P. E. Mogensen, and K. I. Pedersen, "Experimental investigation of correlation properties of MIMO radio channels for indoor picocell scenarios," in *IEEE Vehicular Technology Conference (Fall VTC 2000)*, Boston, MA, Sep 2000, vol. 1, pp. 14–21.

[11] D. P. McNamara, M. A. Beach, P. Karlsson, and P. N. Fletcher, "Initial characterisation of multiple-input multiple-output (MIMO) channels for space-time communication," in *IEEE Vehicular Technology Conference (Fall VTC 2000)*, Boston, MA, Sep 2000, vol. 3, pp. 1193–1197.

[12] J. W. Wallace and M. A. Jensen, "Experimental characterization of the MIMO wireless channel," in *2001 IEEE AP-S Intl. Symposium Digest*, Boston, MA, July 8-13 2001, vol. 3, pp. 92–95.

[13] W. C. Jakes, *Microwave Mobile Communications*, IEEE Press, 1993.

[14] Thomas M. Cover and Joy A. Thomas, *Elements of Information Theory*, John Wiley & Sons, 1991.

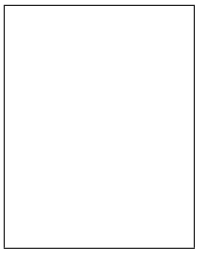

Jon W. Wallace (S'XX, M'XX) received the B.S. (summa cum laude) and Ph.D. degrees in Electrical Engineering from Brigham Young University in 1997 and 2002, respectively. From 1995 to 1997 he worked as an associate of Novell, Inc. in Provo, Utah. During 1997 he was a Member of Technical Staff for Lucent Technologies in Denver, Colorado. He received the National Science Foundation Graduate Fellowship in 1998. From 1998 to 2002 he has worked as a graduate student researcher in the BYU Wireless Communications Laboratory. He is currently a research associate of the BYU Wireless Communications Laboratory and works in Vienna, Austria pursuing joint research with the Technical University of Vienna Mobile Communications Group. His research interests include wireless channel sounding and modeling, optical device modeling, and remote sensing.

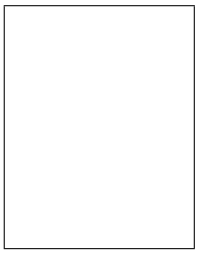

Michael A. Jensen (S'93, M'95, SM'01) received the B.S. (summa cum laude) and M.S. degrees in Electrical Engineering from Brigham Young University (BYU) in 1990 and 1991, respectively, and the Ph.D. in Electrical Engineering at the University of California, Los Angeles (UCLA) in 1994. From 1989 to 1991 he was a graduate research assistant in the Lasers and Optics Laboratory at BYU. In 1990 he received a National Science Foundation Graduate Fellowship. From 1991 to 1994, he was a graduate student researcher in the Antenna Laboratory at UCLA. Since 1994, he has been at the Electrical and Computer Engineering Department at BYU where he is currently an Associate Professor. His main research interests include antennas and propagation for personal communications, microwave circuit design, radar remote sensing, numerical electromagnetics, and optical fiber communications. He is a member of Eta Kappa Nu and Tau Beta Pi.

Dr. Jensen currently serves on the Joint Meetings Committee for the IEEE Antennas and Propagation Society, and served as the Technical Program Chair for the 2000 IEEE International Symposium on Antennas and Propagation. He was awarded the best paper award at the 1994 IEEE International Symposium on Antennas and Propagation.

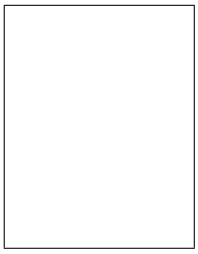

A. Lee Swindlehurst received the B.S., summa cum laude, and M.S. degrees in Electrical Engineering from Brigham Young University, Provo, Utah, in 1985 and 1986, respectively, and the PhD degree in Electrical Engineering from Stanford University in 1991. From 1983 to 1984 he was employed with Eyring Research Institute of Provo, UT, as a scientific programmer. During 1984-1986, he was a Research Assistant in the Department of Electrical Engineering and Brigham Young University, working on various problems in signal processing and estimation theory. He was awarded an Office of Naval Research Graduate Fellowship for 1985-1988, and during most of that time was affiliated with the Information Systems Laboratory at Stanford University. From 1986-1990, he was also employed at ESL, Inc., of Sunnyvale, CA, where he was involved in the design of algorithms and architectures for several radar and sonar signal processing systems. He joined the faculty of the Department of Electrical and Computer Engineering at Brigham Young University in 1990, where he holds the position of Full Professor. During 1996-1997, he held a joint appointment as a visiting scholar at both Uppsala University, Uppsala, Sweden, and at the Royal Institute of Technology, Stockholm, Sweden. His research interests include sensor array signal processing for radar and wireless communications, detection and estimation theory, and system identification.

Dr. Swindlehurst is currently serving as Secretary of the IEEE Signal Processing Society, and is a past Associate Editor for the IEEE Transactions on Signal Processing, a past member of the Statistical Signal and Array Processing Technical Committee in the IEEE Signal Processing Society, and past Vice-Chair of the Signal Processing for Communications Technical Committee within the same society. He has served as the Technical Program Chair for the 1998 IEEE Digital Signal Processing Workshop and for the 2001 IEEE International

Conference on Acoustics, Speech, and Signal Processing. He is also a recipient of the 2000 IEEE W. R. G. Baker Prize Paper Award, and is co-author of a paper that received a Signal Processing Society Young Author Best Paper Award in 2001.

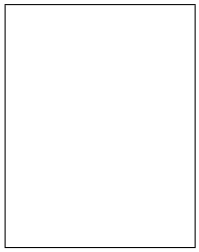

Brian D. Jeffs Brian D. Jeffs received B.S. and M.S. degrees in electrical engineering from Brigham Young University in 1978 and 1982 respectively. He received the Ph.D. degree from the University of Southern California in 1989, also in electrical engineering. He is currently an associate professor in the Department of Electrical and Computer Engineering at Brigham Young University, where he lectures in the areas of digital signal processing, digital image processing, and circuits. Previous employment includes Hughes Aircraft Company in So. California where he served as a sonar signal processing systems engineer in the anti-submarine warfare group. Responsibilities there included algorithm development and system design for digital sonars in torpedo, surface ship towed array, and helicopter dipping array platforms. Current research interests include high data rate digital multiple antenna wireless communications systems, adaptive interference mitigation algorithms for radio astronomy, and blind image restoration.

Dr. Jeffs was a Vice General Chair for IEEE ICASSP-2001, held in Salt Lake City Utah. He was a member of the executive organizing committee for the 1998 IEEE DSP Workshop, and served several years as chair of the Utah Chapter of the IEEE Communications and Signal Processing Societies.

Table Captions

Table I: Measurement system locations within the engineering building along with antenna configurations.

Figure Captions

Figure 1: High level system diagram of the narrowband wireless MIMO measurement system.

Figure 2: Algorithm for recovering the carrier phase.

Figure 3: Plot illustrating the power dynamic range of the receiver system and histogram of the received power level for all measurements used in this analysis.

Figure 4: Empirical PDFs for the magnitude and phase of the 4×4 $\mathbf{H}$ matrix elements compared with Rayleigh and uniform PDFs, respectively.

Figure 5: Empirical PDFs for the magnitude and phase of the 10×10 $\mathbf{H}$ matrix elements compared with Rayleigh and uniform PDFs, respectively.

Figure 6: Temporal correlation coefficient over a 5 second interval for all data sets.

Figure 7: Magnitude of the shift-invariant spatial correlation coefficients at transmit and receive compared with Jakes' model.

Figure 8: CCDFs for 2×2 channels employing different types of polarization/spatial separation.

Figure 9: CCDFs for 2×2 channels employing different types of polarization/spatial separation with realistic normalization.

Figure 10: Capacity CCDFs for 4×4 patches versus 4×4 monopoles.

Figure 11: Capacity CCDFs per number of antennas for transmit/receive arrays of increasing number of elements. The array length is 2.25 λ for all cases.

Figure 12: Study showing the tradeoff between multipath and path-loss with regard to channel capacity. Arrows are drawn from transmit to receive. The top number and bottom number in each box give capacity without and with path loss, respectively.

TABLE I

MEASUREMENT SYSTEM LOCATIONS WITHIN THE ENGINEERING BUILDING ALONG WITH ANTENNA CONFIGURATIONS.

Name	Xmit Loc	Recv Loc	Ant	Records
4×4(a)	RM484	5 Rooms	4SP	233
4×4(b)	Hall	RM400	2DP	165
10×10(a)	Hall	RM400	10SP	474
10×10(b)	RM484	RM400	10SP	137
10×10(c)	Many Rooms	Many Rooms	10SP	120

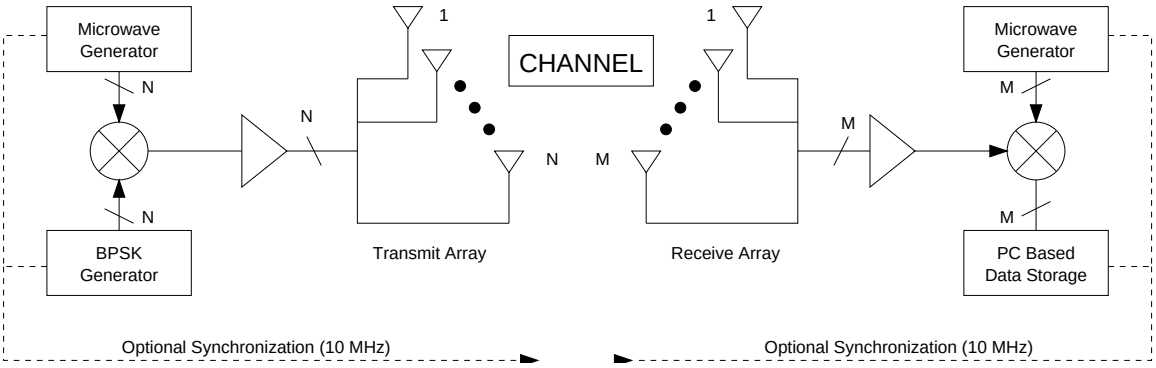

Fig. 1. High level system diagram of the narrowband wireless MIMO measurement system.

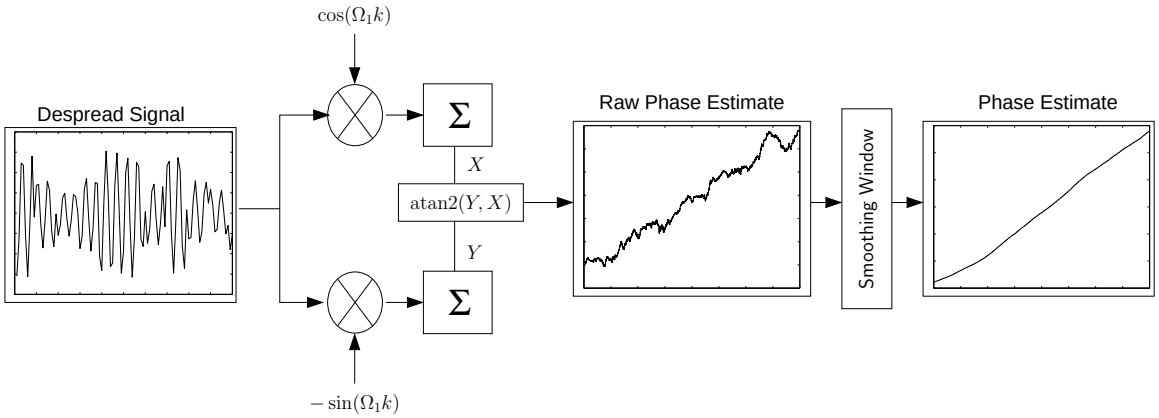

Fig. 2. Algorithm for recovering the carrier phase.

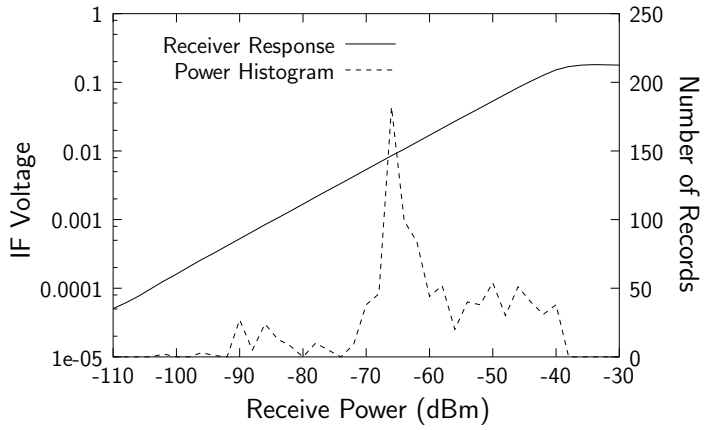

Fig. 3. Plot illustrating the power dynamic range of the receiver system and histogram of the received power level for all measurements used in this analysis.

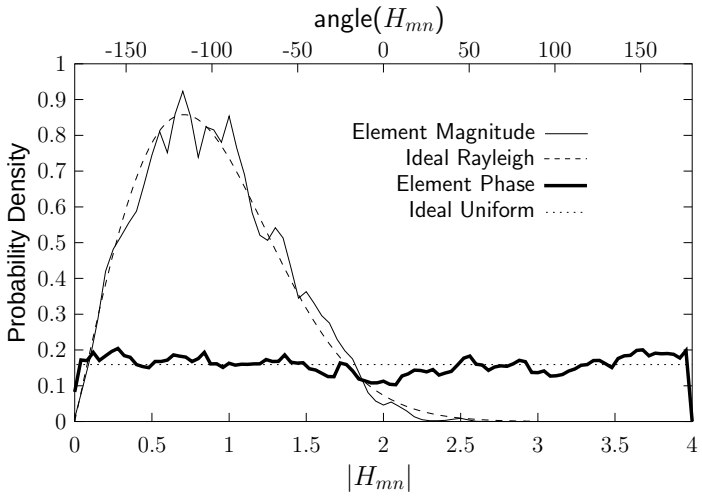

Fig. 4. Empirical PDFs for the magnitude and phase of the 4×4 **H** matrix elements compared with Rayleigh and uniform PDFs, respectively.

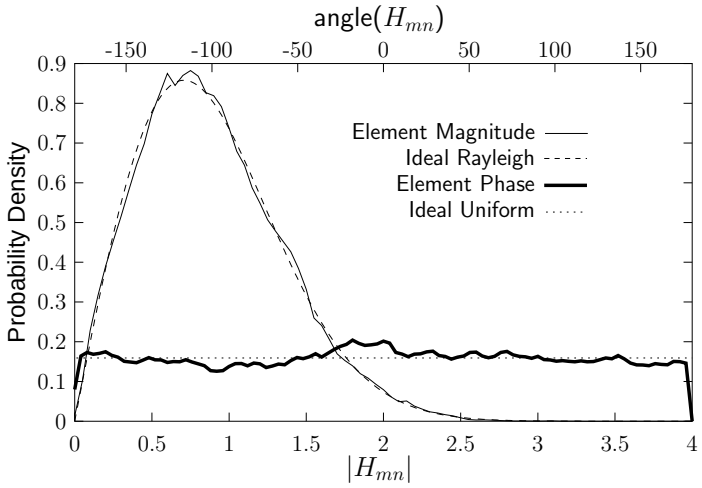

Fig. 5. Empirical PDFs for the magnitude and phase of the 10×10 $\mathbf{H}$ matrix elements compared with Rayleigh and uniform PDFs, respectively.

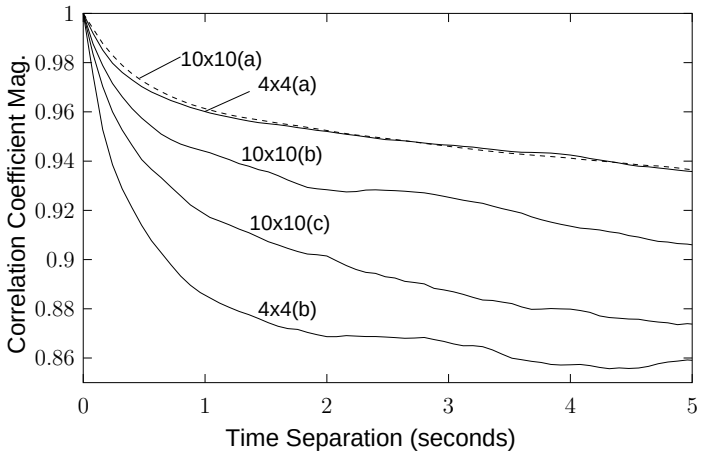

Fig. 6. Temporal correlation coefficient over a 5 second interval for all data sets.

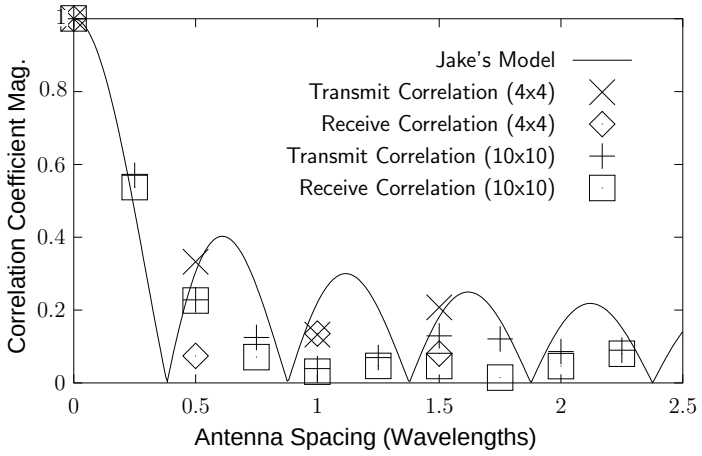

Fig. 7. Magnitude of the shift-invariant spatial correlation coefficients at transmit and receive compared with Jakes' model.

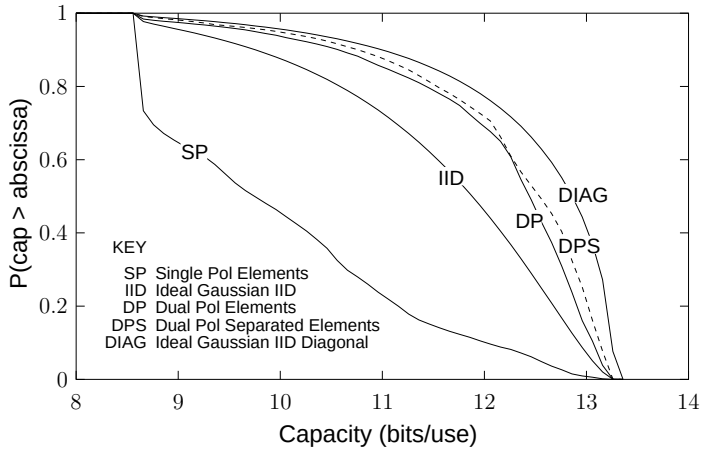

Fig. 8. CCDFs for 2×2 channels employing different types of polarization/spatial separation.

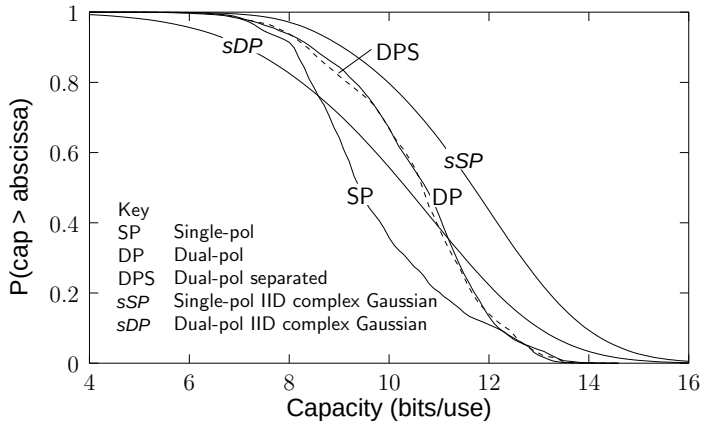

Fig. 9. CCDFs for 2×2 channels employing different types of polarization/spatial separation with realistic normalization.

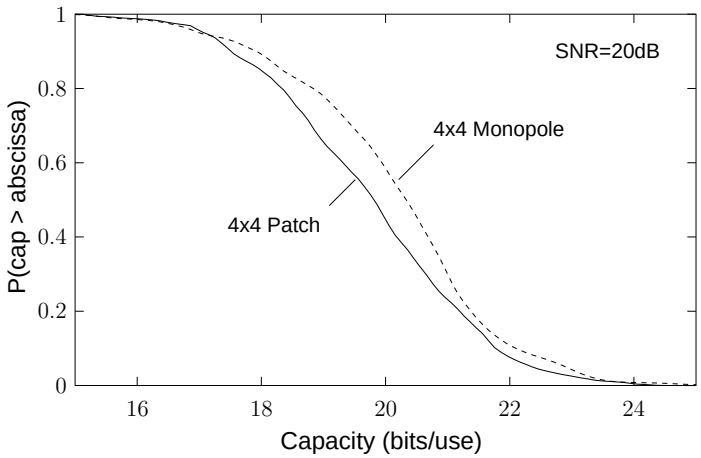

Fig. 10. Capacity CCDFs for 4×4 patches versus 4×4 monopoles.

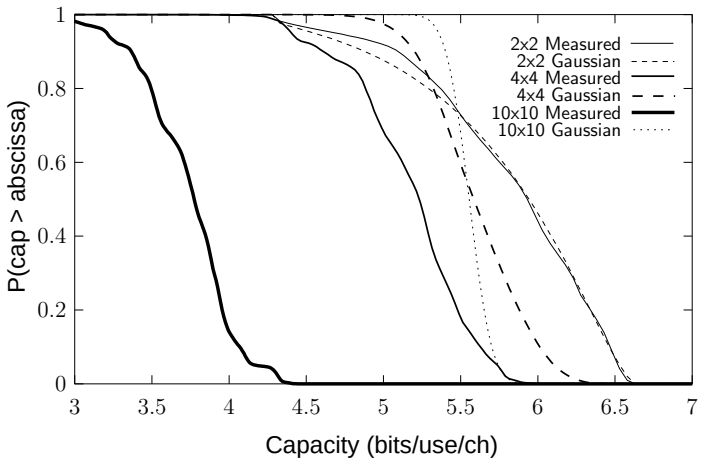

Fig. 11. Capacity CCDFs per number of antennas for transmit/receive arrays of increasing number of elements. The array length is 2.25 λ for all cases.

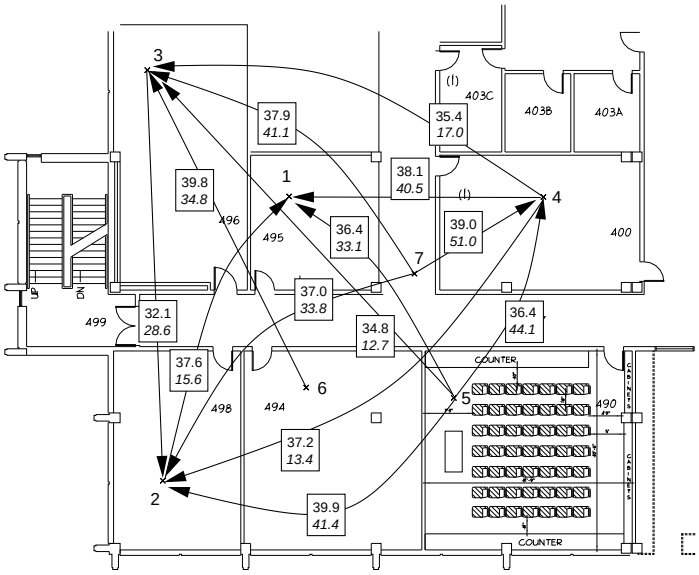

Fig. 12. Study showing the tradeoff between multipath and path-loss with regard to channel capacity. Arrows are drawn from transmit to receive. The top number and bottom number in each box give capacity without and with path loss, respectively.